Phase–field simulation of fractographic features formation in soda–lime glass beams fractured in bending

Lingyue Ma[a], Mostafa Mollaali[b], Roberto Dugnani[a,c,*]

[a] *UM-SJTU Joint Institute, Shanghai Jiao Tong University, Shanghai, China*
[b] *Department of Environmental Informatics, Helmholtz Centre for Environmental Research – UFZ, Leipzig, Germany*
[c] *George R. Brown School of Engineering, Rice University, Houston, TX, USA*

Abstract

The identification of fractographic features, such as the mirror–mist boundary, is central in the fractographic analysis of silicate glasses and other brittle materials. Although phase–field simulations have been previously applied to unstable cracks propagating in amorphous brittle materials, limited efforts have been made to establish the formation of fractographic features. This work proposes two distinct approaches to predict the formation of the mirror–mist boundary in soda–lime glass. Glass beams with embedded corner elliptical notches loaded in bending were considered, and unstable crack propagation was simulated in phase–field. In one approach, the 'mist' was expected to form when the crack–front's speed reached a critical threshold. In the second approach, the thickness of the damaged zone predicted by phase–field was tracked and correlated to the formation of the fractographic features. For the two proposed methods, both the shapes of the estimated mirror–mist boundaries and the magnitudes of the mirror radii were found to be in good agreement with experimental observations gathered from soda–lime glass beams fractured in bending.

Keywords: phase–field, unstable crack, flexural fracture, mirror–mist boundary, silicate glass

1. Introduction

The identification of fractographic features on the fracture surface of amorphous brittle materials, like silicate glasses, are central to fractographers to carry out root cause analysis of the components and estimate their fracture strength. The *mirror*, *mist*, and *hackle* regions form sequentially on the fracture surface of glasses as the crack propagates away from the fracture origin [1], as for instance, shown in Figure 1(a). The optical perception of the 'mist' on the fracture surface is caused by the increase in surface roughness and micro–branching induced by the dynamic stress–field at the crack–tip occurring at high crack velocities [2]. For relatively thick plates fractured in bending or samples fractured in tension, the size of the mirror region, *i.e.*, the mirror radius, R_i, is usually determined along the free surface and correlates with the fracture strength, σ_f, through an empirical function, $\sigma_f = A/\sqrt{R_i}$, where A is the mirror constant [3]. Recently, Dugnani & Zednik [4] and Ma & Dugnani [5] proposed semi–empirical adjustment to this equation to account

*Corresponding author: rdugnani@stanfordalumni.org

for the plate's thickness in plates fractured in flexure although the topic is still debated. In optical fractography, the determination of the mirror–mist boundary is often found subjective and affected by many factors, such as illumination, observing tool, and observers' experience [6, 7, 8]. Efforts have been also made recently in many references to objectively analyze the fracture surface features [5, 9, 10].

Richter [11] suggested that characteristic values of the crack–tip velocity and (static) stress intensity factor (SIF) corresponded to the formation of specific fractographic features on the fracture surface, as shown in Figure 1(b). The formation of fractographic features was expected to correlate with the predominant energy dissipation mode as cracks advance. The crack velocity has been observed to increase rapidly within the mirror region but to keep a nearly uniform speed after the 'mist' formation as a result of the increased energy dissipation due to local micro–cracking [1]. The underlying mechanisms relating the surface feature formation at high crack velocity were discussed by many references, to name a few [12, 13, 14, 15, 16], and some of them are still controversial. However, the high energy and crack speed is considered essential to the formation of the surface features.

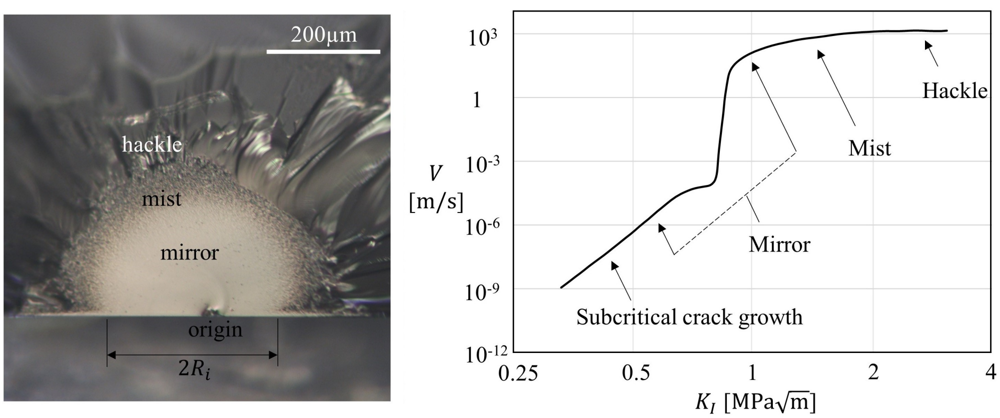

(a) (b)

Fig. 1 (a) Fractograhic features on the glass fracture surface; (b) crack–tip velocity vs. static stress intensity factor and fractographic features (modified from [11])

Due to the difficulty in carrying out experimental studies on unstable cracks, and in the absence of a comprehensive analytical solution to the problem, numerical modeling has become an essential tool to shed light on the crack propagation process. In the past, dynamic crack instabilities, crack path undulation, and crack–branching have been investigated by Spatschek *et al.* [17] using a phase–field approach, by Menouillard & Belytschko [18] with extended finite element method, and by Rabczuk *et al.* [19] with cracking particles method. However, only limited theories to describe the fractographic features' formation on fracture surfaces were put forwards. Kawabata *et al.* [20] predicted the location of the arrest lines in brittle steel using finite element methods. Silling *et al.* [21] analyzed glass rods fractured in tension with peridynamics. Features such as the mirror and the mist were accurately predicted based on the topographic features produced by dynamic crack–tip instabilities. Henry & Adda-Bedia [22] studied the crack–tip splitting instability of fast propagating cracks in brittle solids loaded in tension with phase–field. Local branching at the crack–front was observed and qualitatively correlated to fracture surface features. Fracture surface features were also the focus of fracture animations. For instance, Hahn & Wojtan [23] used boundary element methods to simulate the topography of dynamic brittle fracture based on strength and fracture toughness. Similar work has been carried out by Pauly *et al.* [24], with a meshless method to represent the fracture surface with resampling elliptical splats. These methods reproduced the fracture surface topographies qualitatively but their relation to the actual fractographic features was not verified rigorously.

In the phase–field approach, the crack is represented by a phase–field value. At high crack velocity, larger damaged zones simulated by phase–field are expected at the crack–tip, due to the high–speed instability at the crack–tip, and could be correlated to the fracture surface features [22]. Molnar *et al.* [25] used phase–field in ABAQUS to study dynamic crack branching in brittle materials in mode I. The fracture pattern in both 2D and 3D indicated that the damaged zone increased in the direction perpendicular to the crack propagation direction prior to branching. Borden *et al.* [26] modeled 2D brittle fracture in tension using phase–field, and also in this case the thickness of the damaged zone orthogonal to the crack propagation direction increased prior to branching for the mesh sizes considered. Analogous results were also observed in the 2D phase–field dynamic crack patterns in brittle materials in Hofacker & Miehe [27] and Mehrmashhadi *et al.* [28]. The crack patterns in phase–field were validated by the experimental branching tests of glass, for instance in Mehrmashhadi *et al.* [28]. The regions with increased thickness prior to branching was expected to correspond to the regions with local micro–branching at high crack velocity on real fracture surfaces.

To overcome the difficulties introduced by the crack–tip singularities, this work proposed a numerical approach, using the phase–field analysis, to objectively estimate the formation of the surface features such as the boundaries between the mirror and the mist regions. In this study, soda–lime glass (SLG) beams with quarter–elliptical corner notches loaded by three–point bending tests (3PBT) were modeled. The dynamic crack behavior was analyzed and compared with unstable crack evolution experiments reported in the literature. Following Richter's [11] observations, this approach proposed that the onset of the mist occurred as the crack speed reached a critical threshold. An alternative approach to estimate the mirror–mist boundaries based on the damaged zone predicted in phase–field is also developed. The approach correlated the development of the damaged zone to the formation of surface features, as the result of high–speed instabilities of the propagating cracks.

Section 2 of this manuscript introduces the numerical models used to investigate the dynamic crack propagation, including the phase–field formulation, implementation, and analysis. The methodology proposed to predict the formation of the mirror–mist boundaries based on the crack velocity is also presented. The geometry and loading conditions for the cases simulated are described in Section 3, and experimental testing is presented in Section 4. The expected mirror–mist boundaries are presented in Section 5, and discussed in Section 6. The alternative approach to predict the mirror–mist boundaries based on the damaged zone is described in Appendix A, and a parametric study of the mesh size for the simulations is presented in Appendix B.

2. Numerical methodology

This section introduces the methodology used to analyze unstable crack propagation in SLG by phase–field approach. The formulation of dynamic phase field, implementation, and analysis are also introduced in the section.

2.1. Dynamic variational phase–field approach

2.1.1. Variational formulation of brittle fracture

The problem is solved in a time interval $t \in [0, T]$ in a three–dimensional media occupying an open Lipschitz domain $\Omega \subset \mathbb{R}^3$. Let $\Gamma_D, \Gamma_N \subseteq \partial\Omega$ be such that $\Gamma_D \cup \Gamma_N = \partial\Omega$ and $\Gamma_D \cap \Gamma_N = \emptyset$; $\boldsymbol{u}_D : \Gamma_D \times [0, T] \to \mathbb{R}^3$ and $\boldsymbol{t}_N : \Gamma_N \times [0, T] \to \mathbb{R}^3$ be prescribed displacement and traction boundary conditions, respectively; let $\boldsymbol{b} : \Omega \times [0, T] \to \mathbb{R}^3$ be the body force per unit volume exerted to the solid.

The variational approach to fracture is built on energy minimization with respect to the displacement field $\boldsymbol{u} : \Omega \to \mathbb{R}^3$ and its jump set, which is denoted as $\mathcal{C} = \mathcal{C}(\boldsymbol{u}) \subset \Omega$. Let $|\mathcal{C}|$ denote the one–dimensional Hausdorff measure of $\mathcal{C}$. Following Griffith's theory, the Lagrangian function is written as:

$$\begin{aligned}\mathcal{L}_{\mathcal{C}}\left[\boldsymbol{u}, \dot{\boldsymbol{u}}, \mathcal{C}\right] &:= \Pi_{\texttt{kin}}\left[\boldsymbol{u}, \dot{\boldsymbol{u}}\right] - \Pi_{\mathcal{C}}[\boldsymbol{u}, \mathcal{C}] \\ &:= \int_{\Omega\setminus\mathcal{C}} \left(\frac{1}{2}\rho\dot{\boldsymbol{u}}^{\mathsf{T}}\dot{\boldsymbol{u}} - \psi_0[\boldsymbol{\varepsilon}]\right) \mathrm{d}\Omega - \int_{\Omega} \boldsymbol{b}\cdot\boldsymbol{u}\,\mathrm{d}\Omega - \int_{\Gamma_N} \boldsymbol{t}_N\cdot\boldsymbol{u}\,\mathrm{d}\Gamma + G_c|\mathcal{C}|,\end{aligned} \tag{1}$$

where constant $G_c \in \mathbb{R}^+$ is the strain energy released per unit length of fracture extension. The strain energy density $\psi_0[\boldsymbol{\varepsilon}]$ is given by

$$\psi_0\left(\boldsymbol{\varepsilon}\right) := \frac{\lambda}{2}\left(\mathrm{tr}\,\boldsymbol{\varepsilon}\right)^2 + G\|\boldsymbol{\varepsilon}\|^2, \tag{2}$$

with λ and G Lamé constants. These constants are related to Young's modulus, E, and Poisson's ratio, ν, as $\lambda = E\nu/[(1+\nu)(1-2\nu)]$ and $G = E/[2(1+\nu)]$, $\|\cdot\|$ denotes the Frobenius norm of a tensor.

The linearized strain tensor takes the form:

$$\boldsymbol{\varepsilon}(\boldsymbol{u}) := \frac{1}{2}\left(\nabla\boldsymbol{u} + \nabla\boldsymbol{u}^{\mathsf{T}}\right). \tag{3}$$

2.1.2. Regularized variational formulation of brittle fracture

To develop a numerical method to approximate Eq. (1), the phase–field approach replaces the sharp–fracture description $\mathcal{C}$ with a phase–field description, where the phase–field is denoted as $\mathrm{d} : \Omega \to [0, 1]$. In particular, regions with $d = 0$ and $d = 1$ correspond to the intact and fully broken materials, respectively. Using a phase–field approach, the one–dimensional fracture $\mathcal{C}$ is approximated with the help of an elliptic functional [29, 30]:

$$\mathcal{C}_\ell[d] := \frac{1}{4c_w}\int_\Omega \left(\frac{w(d)}{\ell} + \ell\nabla d\cdot\nabla d\right)\mathrm{d}\Omega, \tag{4}$$

where $\ell > 0$ is the regularization length scale, which may also be interpreted as a material property, *e.g.*, the size of the process zone. Constant $c_w = \int_0^1 \sqrt{w(d)}$ is a normalization constant such that when $\ell \to 0$, $\mathcal{C}_\ell[d]$ converges to the length of the sharp fracture, $|\mathcal{C}|$. Classical examples of $w(d)$ and c_w are $w(d) = d^2$ and $c_w = 1/2$ for the AT_2 model, and $w(d) = d$ and $c_w = 2/3$ for the AT_1 model. Interested readers are referred to [31, 32] for more elaborations.

On this basis, Eq. (1) is replaced by a global constitutive dissipation functional for a rate independent fracture process:

$$\mathcal{L}_\ell\left[\boldsymbol{u},\dot{\boldsymbol{u}},\ell\right]:=\Pi_{\mathtt{kin}}\left[\boldsymbol{u},\dot{\boldsymbol{u}}\right]-\Pi_\ell[\boldsymbol{u},\ell]:=\int_\Omega\left(\frac{1}{2}\rho\dot{\boldsymbol{u}}^{\mathtt{T}}\dot{\boldsymbol{u}}-\psi(\boldsymbol{\varepsilon},d)\right)\,\mathrm{d}\Omega-\int_\Omega\boldsymbol{b}\cdot\boldsymbol{u}\,\mathrm{d}\Omega-\int_{\Gamma_N}\boldsymbol{t}_N\cdot\boldsymbol{u}\,\mathrm{d}\Gamma + \frac{G_c}{4c_w}\int_\Omega\left(\frac{w(d)}{\ell}+\ell\nabla d\cdot\nabla d\right)\mathrm{d}\Omega. \tag{5}$$

Remark 1 (Strain energy degradation)**.** *The solid endures partial loss of stiffness due to the presence of fractures. In order to model this effect, the strain energy density is degraded with respect to the evolution of the phase field. Also note that as the damaged material responds differently to tension and compression, only a part of the strain energy density is degraded. For this purpose, the degraded strain energy in Eq.* (5) *takes the following general form:*

$$\psi(\boldsymbol{\varepsilon},d)=g(d)\psi_++\psi_-, \tag{6}$$

where $g(d)$ satisfies $g(0)=1$, $g(1)=0$, and $g'(d)<0$ for all d such that $0\le d\le 1$ [33]. A usual choice is $g(d)=(1-d)^2+k$. On the other hand, $\psi_\pm$ are such that

$$\psi_+(\boldsymbol{\varepsilon})+\psi_-(\boldsymbol{\varepsilon})=\psi_0(\varepsilon). \tag{7}$$

Now since $\partial\psi/\partial d=g'(d)\psi_+$, only ψ_+ contributes to fracture propagation.

There are several phase–field models that differ in their choice of $\psi_\pm$. In this paper, the one proposed by Miehe *et al.* [34] is adopted. In this model, the negative and positive strain energies read as

$$\psi_\pm[\boldsymbol{\varepsilon}]=\frac{\lambda}{2}\langle\mathrm{tr}\ \boldsymbol{\varepsilon}\rangle_\pm^2+G\sum_{a=1}^{3}\langle\mathrm{tr}\ \boldsymbol{\varepsilon}_a\rangle_\pm^2 \tag{8}$$

where $\{\boldsymbol{\varepsilon}_a\}_{a=1}^3$ are the principal strains.

Remark 2 (Irreversibility constraint)**.** *Miehe* et al. *[34] proposed a phase–field model based on a local history field to model the irreversibility. In this model, the evolution of the phase–field, d, is driven by the historically maximum value of ψ_+ at the point of interest.*

2.2. Implementation of phase–field method for a dynamic crack in ABAQUS

An open–source, implicit, staggered elastodynamic implementation of phase–field approach was developed by Molnar *et al.* [25] aided by a Fortran subroutine code implemented in the commercial finite element analysis software ABAQUS. The approach provided a convenient way of analyzing brittle, dynamic fracture cases using phase–field approach. In Molnar *et al.*'s method, three layers of elements were assigned to the nodes from the 3D mesh. The first layer of elements defined the displacement of the specimen, the second layer defined the fracture topology, *i.e.*, the phase–field value, d, and the third layer added elements with infinitesimally small stiffness to visualize the simulation results in ABAQUS. The simulation results were presented in the solution–dependent variables defined in Molnar *et al.* [25]. Details of the method and phase–field implementation are found in [25, 35].

2.3. Analysis of phase–field simulations

In this work, the dynamic crack propagation in beams with embedded elliptical corner notches loaded in 3PBT was simulated by the phase–field approach. The crack shape and velocity were later used to predict the formation of the mirror–mist boundary.

2.3.1. Crack shape

This work considers unstable cracks extending from the elliptical notch in glass beams loaded in bending. Figure 2 shows a schematic view for a beam of thickness H, width W, and length, L, with an embedded notch at the corner resting on the plane of symmetry (elliptical notch semi–axes, a_0 and c_0; notch thickness, d_0). In the simulations, the cracked surface was defined as the region with phase–field, d, greater than 0.5 [36]. The crack size along the free surface and the side edge were denoted as c and a, respectively (Figure 3).

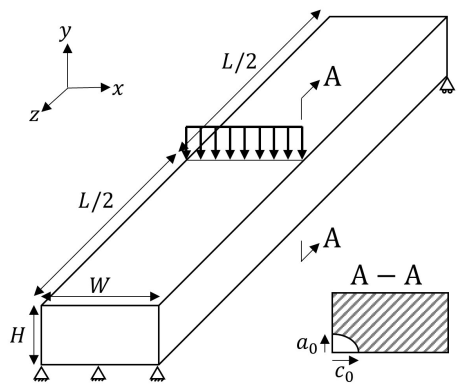

Fig. 2 Geometry and loading conditions for the 3PBT beam

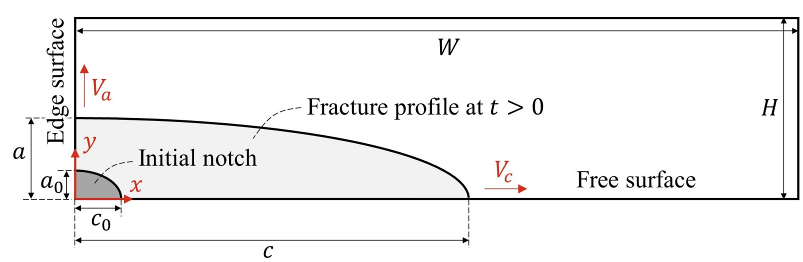

Fig. 3 Schematic view of propagated crack in a plate of thickness H and width W fractured in bending

2.3.2. Critical crack velocity

The crack velocity along the main axes was evaluated at various time steps. The crack velocities along the surfaces, V_c and V_a, at step n was approximated based on adjacent simulation steps $\{n-1, n+1\}$:

$$V_{c,n} = \frac{c_{n+1} - c_{n-1}}{2\mathrm{d}t}, \tag{9}$$

$$V_{a,n} = \frac{a_{n+1} - a_{n-1}}{2\mathrm{d}t}. \tag{10}$$

Figure 4 shows the crack velocity along the free surface, V_c, for the simulation case 3 in Table 1. Based on Richter's [11] observations, in this work the critical velocity, V^*, was defined as the transition velocity between the fast propagating crack characteristic of the mirror region, and the slower propagating crack in the mist/hackle regions, as shown in Figure 4.

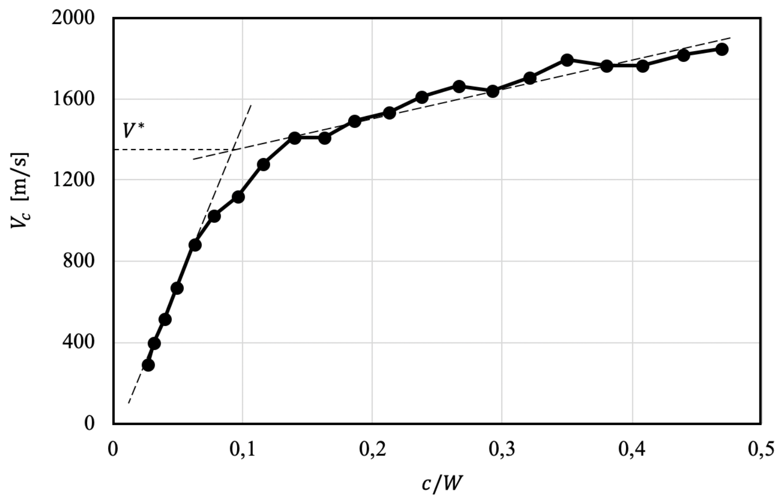

Fig. 4 Crack velocity, V_c, along the free surface versus normalized crack length, c/W, for case 3 in Table 1

2.3.3. The mirror–mist boundary

In this first approach, the mirror–mist boundary was established based on the crack–location as it reached the critical velocity. Figure 5 shows a schematic view of crack–front evolution for a short time step $\mathrm{d}t$. For non–circular cracks, the crack velocity is not uniform along the crack–front. The crack–front velocity was evaluated by first estimating the velocity V_ϕ, in the direction AB in Figure 5. The mirror–mist boundary was predicted to occur when the velocity, V_ϕ, was such that:

$$V_\phi = l_{AB}/\mathrm{d}t = V^*/\cos(\theta - \phi)\,. \tag{11}$$

The mirror–mist boundary was then fitted using a conic section [10] after the location of the boundary was evaluated at various time steps.

3. Numerical experiments

This section describes the numerical examples simulated by the phase–field approach. The beams were model in the computational domains, $\Omega = [0, W] \times [0, H] \times [-L/2, L/2]$ with the origin

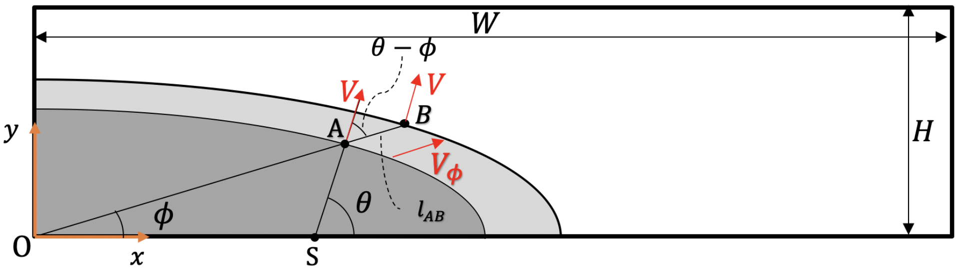

Fig. 5 Schematic view of crack evolution with time step dt

of the coordinate system at the corner of the cross section in the middle of the beam. An quarter elliptical notch at the corner of the specimen was introduced to represent the corner flaws in real samples, $\Gamma = [y^2/a_0^2 + z^2/c_0^2 \leq 1] \times [-d_0/2, d_0/2]$ (Figure 2). Dirichlet boundary conditions of the beam were assigned, such that the simply supported beam was loaded on the top surface in the middle:

$$u_x = u_y = u_z = 0 \quad \text{if} \quad (x, y, z) \in [0, W] \times \{0\} \times \{L/2\}, \tag{12}$$

$$u_x = u_y = 0 \quad \text{if} \quad (x, y, z) \in [0, W] \times \{0\} \times \{-L/2\}, \tag{13}$$

$$u_x = 0 \text{ and } u_z = f(t) \quad \text{if} \quad (x, y, z) \in [0, W] \times \{H\} \times \{0\}, \tag{14}$$

where $f(t)$ is a two–step displacement function:

$$f(t) = \begin{cases} -v_1 \cdot t & \text{if} \quad t \leq t_c, \\ -v_1 \cdot t_c - v_2 \cdot (t - t_c) & \text{if} \quad t > t_c, \end{cases} \tag{15}$$

and t_c is the time that the fracture began to propagate from the notch. The two–step loading function for each case was applied to reduce the computational cost. Simulations initially used a time increment, $\delta t_1 = 2 \times 10^{-6}$ s, at $v_1 = 10^3$ mm/s; and as the crack started to propagate, $\delta t_2 = 1 \times 10^{-8}$ s, at $v_2 = 10^2$ mm/s.

A mesh with four–node tetrahedral element (type C3D4) was generated on the beam with the finest, effective mesh size, h, assigned near the symmetric plane at $z = 0$, and coarse mesh was assigned with linearly increasing size from the notch towards the end of the beam until the size $0.25H$ was reached. The regularization length scale was selected equal to the finest mesh size in each simulation, i.e., $\ell = h$. The notch size in each case was $d_0 = 2h$. The magnitudes of h and ℓ were selected to achieve various fracture strengths in the simulations, since the fracture strength $\sigma_f = \sqrt{3G_cE/8\ell}$ (material properties see below) for tensile AT_1 model in phase–field [37]. An overview of the 3D mesh is shown in Figure 6. The effective mesh size is 0.01 mm while the coarsest mesh size is 0.25 mm. The effective mesh normalized with the beam geometry was $h/H = 0.01$. The notch size $d_0 = 0.02$ mm.

Twenty–one numerical scenarios corresponding to the beam geometries and notch sizes described in Table 1 were simulated. The ratio of W/H ranged between 1 and 20. Typical material properties for SLG are shown in Table 2.

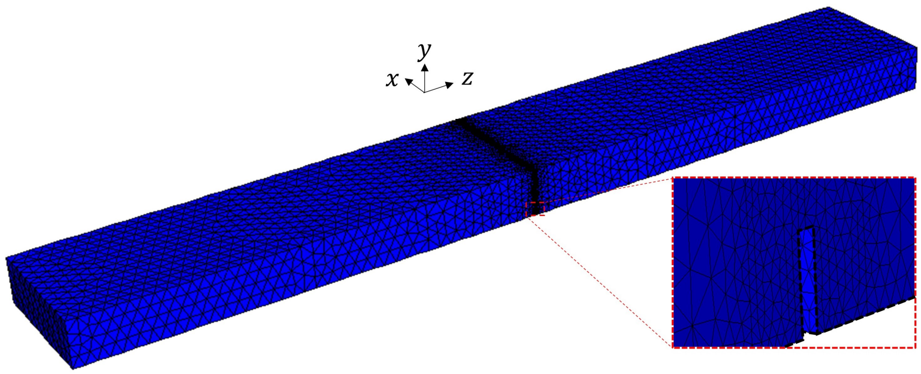

Fig. 6 Overview of 3D meshes for a beam of thickness $H = 1$ mm, with 49,915 nodes and 273,454 elements (C3D4 tetrahedral element). Effective mesh size $h = 0.01$ mm, coarsest mesh size 0.25 mm

Table 1 Geometry conditions, simulated strength, and mirror radius for numerical cases

Case No.	L [mm]	H [mm]	W [mm]	c_0 [mm]	a_0 [mm]	d_0 [mm]	h [mm]	t_c [10^{-4}s]	σ_f [MPa]	R_i [mm]
1	20	1	3	0.07	0.05	0.02	0.01	1.1	125	0.37
2	20	6	6	0.06	0.05	0.02	0.01	0.4	181	0.14
3	20	1	3	0.04	0.03	0.01	0.005	1.6	163	0.32
4	20	1	11	0.45	0.18	0.06	0.03	1.1	86	1.20
5	20	1	3	0.07	0.05	0.02	0.01	0.8	151	0.26
6	20	1	3	0.08	0.06	0.04	0.02	1.6	86	0.35
7	20	1	5	0.20	0.15	0.04	0.02	0.6	88	0.65
8	20	1	5	0.20	0.15	0.04	0.02	0.6	79	0.91
9	20	1	5	0.20	0.15	0.04	0.02	0.6	79	0.82
10	20	1	6	0.20	0.15	0.04	0.02	0.4	81	1.10
11	20	1	6	0.20	0.15	0.04	0.02	0.5	81	0.91
12	20	1	6	0.45	0.18	0.06	0.03	1.1	58	1.95
13	20	1	6	0.47	0.25	0.06	0.03	0.6	63	1.32
14	20	1	6	0.20	0.15	0.04	0.02	0.6	81	0.94
15	20	1	7	0.20	0.15	0.04	0.02	0.6	88	0.53
16	20	1	7	0.20	0.15	0.04	0.02	0.6	88	1.62
17	20	1	11	0.45	0.20	0.16	0.08	1.1	56	1.64
18	20	1	12	0.45	0.18	0.06	0.03	1.1	61	1.23
19	20	1	12	0.45	0.18	0.06	0.03	1.1	61	1.29
20	20	1	13	0.45	0.18	0.06	0.03	0.6	83	1.23
21	20	1	20	0.45	0.18	0.08	0.04	1.1	61	1.86

4. Experimental testing

Various experimental tests were carried out to validate the numerical results. 2 mm–thick SLG plates were fractured by four-point bending tests (4PBT) using an MTS universal testing machine

Table 2 Material properties for *soda-lime glass*

Name	Symbol	Value	Unit	Ref.
Young's modulus	E	72×10^3	MPa	[38]
Critical energy release rate†	G_c	6.8×10^{-3}	MPa·mm	[39]
Density	ρ	2.5×10^3	kg/m^3	[38]
Poisson's ratio	ν	0.25	–	[38]

$^\dagger G_c = K_{Ic}^2/E$.

(model C45, load resolution 0.01 N). Adhesive tape was attached to the compressive side of the plates to collect the fractured shards after fracture. The outer and inner spans were 200 mm and 100 mm, and rollers' diameter was 10 mm. The 4PBT was applied based on ASTM C158 [40], with loading rate 0.01mm/s (stressing rate 0.15MPa/s). More details of the experimental test could be referred to in [40]. An image of the fixture is shown in Figure 7(a).

In the numerical simulation, the bending stress field on the plane of crack propagation was generated with 3PBT. The experimental validation was performed with 4PBT as recommended in [40], due to the distribution of natural flaws in experimental samples. However, both 3PBT and 4PBT generated mode-I bending stress field at the crack plane, hence they were considered equivalent in this work. Moreover, the results from the numerical and experimental tests were correlated by the fracture surface features, where identical shape of the mirror region should correspond to the same stress field at fracture according to the dimension analysis [5, 10].

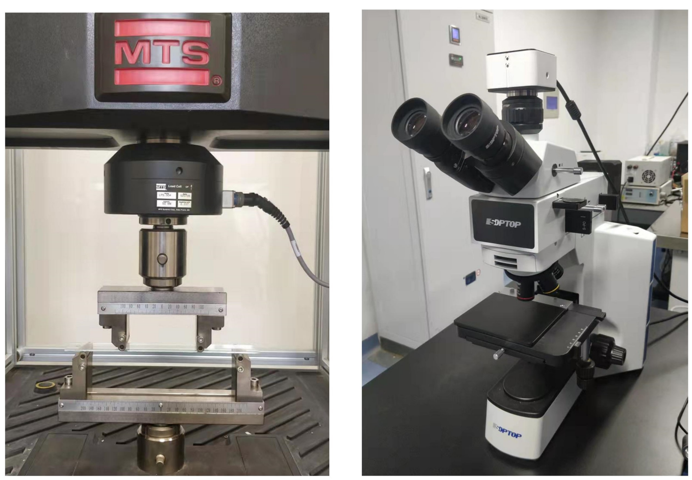

(a) (b)

Fig. 7 (a) MTS setup for 4PTB, (b) optical microscope SOPTOP ICX41M

5. Results and validation

This section presents the phase–field simulation results for SLG flexural beams with an initial notch at the corner. The evolution of the crack along the free surfaces was compared to the experimental findings in Sherman & Be'ery [41] for glass plates fractured in bending.

Fracture surface features such as the mirror–mist boundary, were established based on the critical crack velocity, V^*, and compared with the fracture surfaces of SLG samples produced experimentally.

5.1. Fracture surface features

The fracture surface of SLG beams tested experimentally were examined by optical microscope (SOPTOP ICX41M, Figure 7(b)). Figure 8(a) shows a fractured beam with the crack originating at the side edge, and the corresponding fracture surface is shown in Figure 8(b). The boundary between the mirror and the mist region is highlighted in the figure by the blue dotted line.

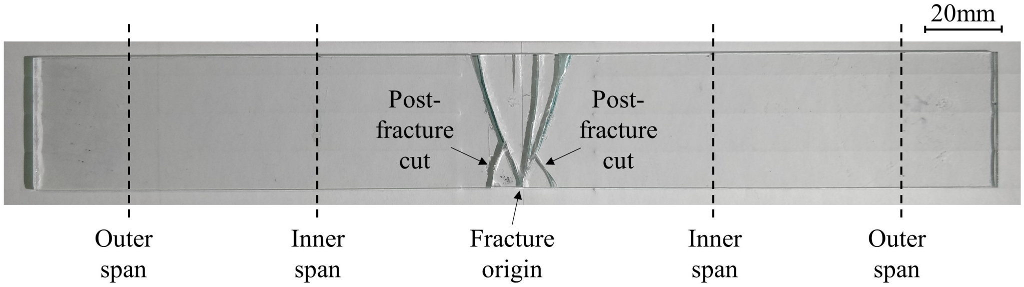

(a)

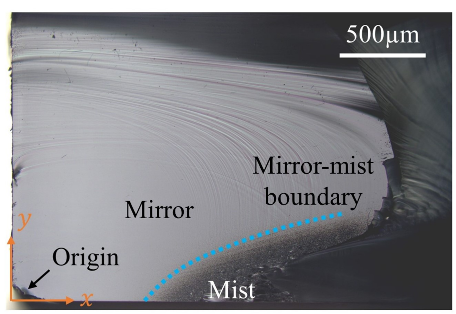

(b)

Fig. 8 (a) An example of fracture pattern of SLG beam in 4PTB, and (b) image of the fracture surface near the origin

5.2. Numerical simulations

5.2.1. Crack pattern in phase–field

Figure 9 shows an instance of crack propagation from an elliptical corner notch simulated by phase–field, d at $z = 0$ and the magnitude of the stress normal to the plane of symmetry, σ_{zz}, at five time steps.

5.2.2. Crack aspect ratio evolution

The evolution of the crack aspect ratio, a/c, with respect to the normalized crack length, c/H, for cases 1 to 4 is presented in Figure 10. On the same figure, the experimental results reported in Sherman & Be'ery [41] are plotted with a solid line. Sherman & Be'ery measured the evolution of the crack for a glass plate ($H = 6$ mm and $W = 60$ mm) fractured in bending using a *potential drop* method [42].

5.2.3. Crack velocity along the free surface

Figure 11 shows the crack velocity along the free surface, V_c, estimated through Eq. (9) versus c/W, for cases 1 to 4 in Table 1. The corresponding experimental results reported in Sherman & Be'ery [41] are shown in the same figure. The estimated average magnitude of V^* for the simulated cases was 1496±220 m/s.

5.3. The mirror–mist boundaries

The boundaries between the mirror and the mist regions were predicted based on the critical crack velocity, V^*, defined in Section 2.3.2. The mirror–mist boundaries estimated at $V = V^*$, for cases 1 to 4 in Table 1, are shown as the white dotted lines in Figure 12(a) to 12(d), and the areas corresponded to the mist region are shaded. The mirror radius, R_i, was then determined along the free surface, as shown in Figure 12(a).

Experimental validation was conducted with SLG specimens fractured in 4PBT. The fractured beams were selected with a similar value of the normalized mirror radius, R_i/H. For instance, $R_i/H = 0.37$ from the simulation in Figure 12(a), while $R_i/H = 0.36$ for the experimental sample in Figure 12(e). The mirror–mist boundaries in Figure 12(e) to 12(h) were visually determined following the fractographic guidelines in ASTM C1678 [3], and highlighted by white dotted lines.

5.3.1. Fracture strength and mirror radius

The fracture strengths were assumed to be equal to the maximum tensile stress induced on the free surface when the crack started propagating. The magnitudes of the strength and the estimated mirror radius for each case are summarized in Table 1. Figure 13 shows a plot of the dimensionless groups $\sigma_f \sqrt{H/K_{Ic}}$ versus $\sqrt{H/R_i}$, for the twenty-one simulated scenarios following the analysis of Ma & Dugnani [5] for flexural fractures. On the same plot, the trend proposed by Ma & Dugnani [5] is also shown.

6. Discussion

In this work, phase–field analysis was used to investigate the crack propagation and the formation of the mist region on the fracture surface of SLG fractured in bending. The numerical simulations implemented in this work focused on only isotropic, elastic solids. Numerical simulations were run with the commercial finite element software ABAQUS with the Fortran subroutine code developed by Molnar *et al.* [25]. The crack front was assumed to correspond to the value of the phase field parameter $d = 0.5$.

In one approach used in this work, the formation of the mist region in SLG samples was assumed to correspond to a critical value of the crack-front's velocity, as suggested by Richter [11]. While the second approach predicted the onset of mist region based on the increased thickness of the damaged zone, as described in Appendix A.

6.1. Unstable crack evolution validation

Figure 10 shows the crack aspect ratio, a/c, versus c/H and includes the experimental results obtained from fractured glass plates reported by Sherman & Be'ery [41]. The difference in the crack growth performance among the four cases was due to the difference in notch sizes and/or beam geometries at the initial stage of the propagation. The crack aspect ratio, a/c, converged to the same trend as the crack extended to $c/H > 2$, similar to the behavior in SLG plates fractured in bending reported by Sherman & Be'ery [41]. The better agreement between the experimental trend from Sherman and Be'ery and case 4 is possibly due to similar beam geometries ($W/H = 11$).

6.2. Crack velocity

The crack velocity along the free surface, V_c, was obtained at various time steps, and plotted as a function of c/W for the cases 1 to 4 reported in Table 1. As shown in Figure 11, the crack velocity increased rapidly at the initial stage for $c/W < 0.1$. For $c/W > 0.1$, additional energy dissipation sinks, such as micro–branching and micro–cracking, become increasingly significant [16, 43, 44, 45]. When the crack propagated farther, at $c/W > 0.5$, inconsistent trends for the crack velocity were observed possibly due to the differences in the loading conditions, sample geometry, and mesh size. Hence this work mainly focused on crack speed at $c/W < 0.5$.

Experimental measurements of the crack speed in SLG indicated that the crack initially expanded rapidly and subsequently reached a stage with nearly uniform 'terminal velocity' [46] as shown for instance in Sherman & Be'ery [41] (Figure 11). However, in the simulated cases, no velocity plateau was observed when $V > V^*$, suggesting that the mist might form before the 'terminal velocity' is reached. As discussed in the NIST guideline [1], the mist in glasses is formed by local deviations of the crack front out of plane. The mist region consumes additional energy and retards crack velocity. In this work, the simulated critical velocity, V^*, was 1496$\pm$220 m/s, consistent with the reported speed corresponding to mirror–mist transition in SLG, 1500$\sim$1600m/s [11, 47, 48].

6.3. The mirror–mist boundary based on crack velocity

In this work, the mirror–mist boundary was assumed to occur as the crack velocity reached a critical value, V^*, as explained in previous sections. The crack velocity along the crack–front as a function of the angle, ϕ, was obtained from the numerical simulations and the location of the mist region was established through Eq. (11). To minimize errors, the time interval between crack fronts, dt, was chosen so that the difference in crack shapes between two adjacent crack–fronts was small but distinct.

The estimated mirror–mist boundaries obtained from representative simulations are shown in Figure 12. The corresponding mirror–mist boundaries from optical images of the fracture surfaces in SLG specimens are shown in the same figure. The experimental results were chosen with similar normalized mirror radius, R_i/H. Based on previous studies by Dugnani & Zednik [4, 10] and Johnson & Holloway [49], samples sharing the same normalized mirror radius, R_i/H, display the same shape of the mirror–mist boundary. A comparison of the mirror–mist boundaries in Figure 12 suggest good agreement especially near the free surface (see also Figure 16). The difference between the shape of the mirror–mist boundaries might be due to numerical inaccuracies such as mesh size, regularization length and computational time increments.

6.3.1. The mirror–mist boundary based on damaged zone

The second approach to predict the mirror–mist boundary was based on the evolution of the damaged zone's thickness during crack extension simulated by phase–field, and is described in Appendix A. The damaged zone simulated by phase–field does not refer to the volume or topography of the real crack, its thickness mainly depend on the regularization length scale, ℓ. However, the evolution of the damaged zone is likely correlated to the crack–tip's instabilities in the mist region. The approach was successful in estimating the shape of the mirror–mist boundary, and could be used as supporting evidence for fractographic features analysis using phase–field. Although more accurate results could be obtained with finer mesh size, the computational cost would significantly increase.

6.4. Crack strength and mirror radius

The normalized fracture strength, $\sigma_f\sqrt{H/K_{Ic}}$ versus $\sqrt{H/R_i}$, is plotted in Figure 13 for all the simulated cases. On the same plot, the trend corresponding to flexural fractures in brittle materials reported by Ma & Dugnani [5] is also shown. The error between the numerical results and the trend reported in Ma & Dugnani was on the average 7%. It could be concluded that the numerical simulations in this work leads to accurate estimation of the mirror radius, for R_i/H ranging from 0.14 to 1.86. Regretfully no fracture resulting in a very long mirror radius, $R_i/H \gg 1$, could be simulated in this work as the finite notch width did not introduce a high stress singularity. It follows that the effect from sample's thickness on the mist formation described in [4, 5] could not be independently verified in this study. The strength versus the inverse of the square root of the mirror radius could also be regressed with the equation $\sigma_f = A/\sqrt{R_i} + C$, with $A = 1.7$ MPa$\cdot\sqrt{\text{m}}$, $C = 22$ MPa leading to average 4% strength differences between the estimations and the numerical results. The magnitude of A for SLG plates obtained from the numerical study, was found to be marginally larger than the magnitudes reported for SLG of similar thickness (*e.g.* $A = 1.4$ MPa$\cdot\sqrt{\text{m}}$ for samples with $H = 1$ mm [50]), but in line with the magnitudes of the mirror constant from other authors [5, 51, 52].

7. Conclusions

This work was aimed at developing a relationship between the fracture strength and characteristic length scale such as the mirror–mist radius on the fracture surface of soda–lime silicate glass. Phase–field numerical simulations were carried out to analyze unstable cracks in isotropic, elastic materials. The phase–field approach was implemented from an open–source subroutine in ABAQUS, and beams with corner elliptical notches loaded in 3PBT were modeled, and later validated with the experimental crack extension information available in the literature.

In this work, the mirror-mist boundary was assumed to occur in the last portion of the initial fast accelerating stage of the crack propagation based on experimental evidence reported in the literature. A novel approach combing phase–field simulations with the formation of the mirror-mist boundary was proposed. The shape of the mirror–mist boundary predicted numerically was in excellent agreement with the observed fracture surface features observed on fractured glass plates, and the predicted fracture strength versus mirror radius trend was on the average within 7% from average values reported in the literature. An alternative approach to interpret the mirror–mist boundary was also developed based on the thickness of the damaged zone. Although affected by the modeling and simulation parameters, like mesh size and regularization length, the alternative approach was able to provide a good visual representation of the fracture surface features without significant post-processing. Both the approaches proposed in this work were successful in predicting the mirror–mist boundaries on soda–lime glass plates fractured in bending, and in the future they could be extended to carry out computer-aided fractographic analyses of brittle materials, for components of any user–defined geometry and material properties.

Appendix A The mirror–mist boundary based on damaged zone

This appendix introduces an alternative approach to estimate the mirror–mist boundary based on the phase–field's damaged zone. The approach provides a novel view analyzing the result of phase–field simulation, building an intuitive connection between phase–field damage and fracture surface features.

In the phase–field simulation, the crack–front was defined by the location where $d = 0.5$. The thickness of the damaged zone (with $d > 0.5$) in the direction orthogonal to the crack propagation, was denoted as Δz, as shown in Figure 14(a). In the numerical simulations, the thickness of the damaged zone was observed to increase with respect to the reference magnitude near the notch, denoted as Δz_0 as shown in Figure 14(b). Δz_0 was defined within the mirror region as

$$\Delta z_0 \equiv \Delta z \quad \text{at} \quad (x, y) = (c_0, a_0). \tag{16}$$

The width of the damaged zone, Δz, in the phase–field simulation was a numerical outcome related to the regularization length scale, ℓ. Although hard to build the relation between Δz and the physical values in the fracture process, its magnitude increased, i.e., $\Delta z/\Delta z_0 \geq 1$, as crack advanced in all simulation cases, since phase-field was successful in predicting the dynamic instability at the crack–tip [22]. In this work, the mirror–mist boundary was arbitrarily set to occur at $\Delta z/\Delta z_0 = 1.5$.

Figure 15 shows the magnitude of the ratio $\Delta z/\Delta z_0$ for cases 1 to 4 in Table 1. Although the damaged zone depends on the effective mesh size, h, similarities were observed in the behavior of the ratio $\Delta z/\Delta z_0$ as the crack grew. The regions corresponding to $\Delta z/\Delta z_0 < 1.5$ were shaded in light gray and the mirror–mist boundary was assumed to occur at $\Delta z/\Delta z_0 = 1.5$, and highlighted with red, dotted lines. In Figure 15(f) to 15(i), the experimental fracture surfaces with similar R_i/H as the simulated ones, were shown for comparison, and the estimated mirror–mist boundaries were highlighted with red, dotted lines. Figure 16 compares the mirror–mist boundaries estimated from the phase–field with the thickness of the damaged zone, $\Delta z/\Delta z_0 = 1.5$ (red), with the critical velocity, $V = V^*$ (white), and the boundaries obtained from fractographic analysis (blue), for the four cases considered. Differences were expected between the approach based on the thickness of the damaged zone and experimental observations, due to the influences from the simulation parameters, such as effective mesh size, h, regularization length scale, ℓ, etc.

Appendix B Parametric study on ℓ/h

In the manuscript, the shape of mirror–mist boundary was investigated with the phase–field method. In the current appendix, the effect of the mesh size on the numerical outputs was studied.

A separate case was studied with the properties: $H \times W \times L = 1$ mm$\times$3 mm$\times$20 mm; $c_0 = 0.07$ mm, $a_0 = 0.05$ mm, $d_0 = 2h$; $\ell = 0.02$ mm. Four mesh sizes were assigned near the expected crack path at the center of the beam in four separate simulations: $h = 0.02$ mm, 0.01 mm, 0.005 mm, and 0.0025 mm, resulting in ℓ/h =1, 2, 4, and 8.

The mirror–mist boundaries were analyzed using the proposed approaches in this manuscript. The results estimated based on the crack velocity for various ℓ/h are shown in Figure 17; and the results estimated based on the normalized thickness of the damaged area, $\Delta z/\Delta z_0$, are shown in Figure 18. In both Figures 17 and 18, the simulation with various ℓ/h resulted in similar estimated mirror–mist boundaries. The slight variations observed in each case could be attributed to the difference in the mesh structures in corresponding simulation cases.

Declaration of competing interest

The authors declare that they have no known competing financial interests or personal relationships that could have appeared to influence the work reported in this work.

References

[1] G. Quinn, NIST Recommended Practice Guide: Fractography of Ceramics and Glasses, 3rd edition, 2020.

[2] E. H. Yoffe, The moving griffith crack, The London, Edinburgh, and Dublin Philosophical Magazine and Journal of Science 42 (1951) 739–750.

[3] ASTM, Standard practice for fractographic analysis of fracture mirror sizes in ceramics and glasses, ASTM Standard C1678 (2015).

[4] R. Dugnani, R. Zednik, Flexural strength by fractography in modern brittle materials, Journal of the American Ceramic Society 96 (2013) 3908–3914.

[5] L. Ma, R. Dugnani, Fractographic analysis of silicate glasses by computer vision, Journal of the European Ceramic Society 40 (2020) 3291–3303.

[6] L. Ma, R. Dugnani, R. Zednik, Quantifying the accuracy of fractographic strength estimates in silicate glasses, Journal of the European Ceramic Society 38 (2018) 3643–3649.

[7] L. Ma, D. Djurdjanovic, R. Dugnani, Statistical accuracy of fractographic estimation in silicate glasses with design of experiments and pairwise t-tests, Engineering Failure Analysis 116 (2020) 104699.

[8] J. J. Swab, G. Quinn, Fractography of Advanced Structural Ceramics: Results from the VAMAS Round Robin Exercise., Technical Report, Army Research Lab Watertown MA Materials Directorate, 1994.

[9] L. Ma, R. Dugnani, Improved fractographic strength estimates based on surface profilometry, in: MATEC Web of Conferences, volume 166, EDP Sciences, 2018, p. 01005.

[10] R. Dugnani, R. J. Zednik, Geometric description of fracture surface features in isotropic brittle solids, Engineering Fracture Mechanics 165 (2016) 87–97.

[11] H. Richter, Fractography of bioceramics, in: Key Engineering Materials, volume 223, Trans Tech Publ, 2002, pp. 157–180.

[12] B. Lawn, Fracture of Brittle Solids, Cambridge Solid State Science Series, 2 ed., Cambridge University Press, 1993.

[13] L. Ma, R. Dugnani, Analytical description of unstable, rugose, circular cracks in brittle solids, Archive of Applied Mechanics 92 (2022) 3923–3941.

[14] H. P. Kirchner, Brittleness dependence of crack branching in ceramics, Journal of the American Ceramic Society 69 (1986) 339–342.

[15] D. Hull, Fractography: Observing, Measuring and Interpreting Fracture Surface Topography, 1999.

[16] M. J. Buehler, H. Gao, Dynamical fracture instabilities due to local hyperelasticity at crack tips, Nature 439 (2006) 307–310.

[17] R. Spatschek, M. Hartmann, E. Brener, H. Müller-Krumbhaar, K. Kassner, Phase field modeling of fast crack propagation, Physical Review Letters 96 (2006) 015502.

[18] T. Menouillard, T. Belytschko, Dynamic fracture with meshfree enriched XFEM, Acta mechanica 213 (2010) 53–69.

[19] T. Rabczuk, J.-H. Song, T. Belytschko, Simulations of instability in dynamic fracture by the cracking particles method, Engineering Fracture Mechanics 76 (2009) 730–741.

[20] T. Kawabata, A. Inami, S. Aihara, Numerical model of brittle crack propagation considering fracture surface energy on high tensile strength steel–proposal of a numerical model of brittle crack propagation (Report 1), Journal of the Japan Society of Naval Architects and Ocean Engineers 16 (2012).

[21] S. A. Silling, F. Bobaru, Y. Wang, Three–Dimensional Simulation of Fractographic Features with Multiscale Peridynamics., Technical Report, Sandia National Lab.(SNL–NM), Albuquerque, NM (United States), 2015.

[22] H. Henry, M. Adda-Bedia, Fractographic aspects of crack branching instability using a phase-field model, Physical Review E 88 (2013) 060401.

[23] D. Hahn, C. Wojtan, High–resolution brittle fracture simulation with boundary elements, ACM Transactions on Graphics (TOG) 34 (2015) 1–12.

[24] M. Pauly, R. Keiser, B. Adams, P. Dutré, M. Gross, L. J. Guibas, Meshless animation of fracturing solids, ACM Transactions on Graphics (TOG) 24 (2005) 957–964.

[25] G. Molnar, A. Gravouil, R. Seghir, J. Réthoré, An open–source Abaqus implementation of the phase–field method to study the effect of plasticity on the instantaneous fracture toughness in dynamic crack propagation, Computer Methods in Applied Mechanics and Engineering 365 (2020) 113004.

[26] M. J. Borden, C. V. Verhoosel, M. A. Scott, T. J. Hughes, C. M. Landis, A phase-field description of dynamic brittle fracture, Computer Methods in Applied Mechanics and Engineering 217 (2012) 77–95.

[27] M. Hofacker, C. Miehe, A phase field model of dynamic fracture: Robust field updates for the analysis of complex crack patterns, International Journal for Numerical Methods in Engineering 93 (2013) 276–301.

[28] J. Mehrmashhadi, M. Bahadori, F. Bobaru, Comparison of peridynamic and phase-field models for dynamic brittle fracture in glassy materials (2020).

[29] L. Ambrosio, V. M. Tortorelli, Approximation of functional depending on jumps by elliptic functional via t–convergence, Communications on Pure and Applied Mathematics 43 (1990) 999–1036.

[30] L. Ambrosio, V. M. Tortorelli, On the approximation of free discontinuity problems (1992).

[31] E. Tanné, T. Li, B. Bourdin, J.-J. Marigo, C. Maurini, Crack nucleation in variational phase–field models of brittle fracture, Journal of the Mechanics and Physics of Solids 110 (2018) 80–99.

[32] B. Bourdin, J.-J. Marigo, C. Maurini, P. Sicsic, Morphogenesis and propagation of complex cracks induced by thermal shocks, Physical Review Letters 112 (2014) 014301.

[33] B. Bourdin, G. A. Francfort, J.-J. Marigo, Numerical experiments in revisited brittle fracture, Journal of the Mechanics and Physics of Solids 48 (2000) 797–826.

[34] C. Miehe, M. Hofacker, F. Welschinger, A phase field model for rate–independent crack propagation: Robust algorithmic implementation based on operator splits, Computer Methods in Applied Mechanics and Engineering 199 (2010) 2765–2778.

[35] Y. Shen, M. Mollaali, Y. Li, W. Ma, J. Jiang, Implementation details for the phase field approaches to fracture, Journal of Shanghai Jiaotong University (Science) 23 (2018) 166–174.

[36] H. Henry, Study of the branching instability using a phase field model of inplane crack propagation, EPL (Europhysics Letters) 83 (2008) 16004.

[37] T. K. Mandal, V. P. Nguyen, J.-Y. Wu, Length scale and mesh bias sensitivity of phase-field models for brittle and cohesive fracture, Engineering Fracture Mechanics 217 (2019) 106532.

[38] Abrisa Technologies, Specialty Glass Materials Products and Specifications 10/21, Technical Report, 2021.

[39] D. Harding, W. Oliver, G. Pharr, Cracking during nanoindentation and its use in the measurement of fracture toughness, MRS Online Proceedings Library (OPL) 356 (1994).

[40] ASTM, Standard test methods for strength of glass by flexure, ASTM Standard C158 (2017).

[41] D. Sherman, I. Be'ery, Shape and energies of a dynamically propagating crack under bending, Journal of Materials Research 18 (2003) 2379–2386.

[42] B. Stalder, P. Béguelin, H. Kausch, A simple velocity gauge for measuring crack growth, International Journal of Fracture 22 (1983) R47–R50.

[43] J. Craggs, The growth of a disk–shaped crack, International Journal of Engineering Science 4 (1966) 113–124.

[44] J. Eshelby, Inelastic behavior of solids, Ed Kanninen (1970) 77–115.

[45] H. Schardin, et al., Velocity effects in fracture, Fracture (1959) 297–330.

[46] J. Fineberg, The dynamics of rapidly moving tensile cracks in brittle amorphous material, in: Dynamic fracture mechanics, World Scientific, 2006, pp. 104–146.

[47] R. C. Bradt, The fractography and crack patterns of broken glass, Journal of failure analysis and prevention 11 (2011) 79–96.

[48] M. Adda-Bedia, M. B. Amar, Y. Pomeau, Morphological instabilities of dynamic fractures in brittle solids, Physical Review E 54 (1996) 5774.

[49] J. Johnson, D. Holloway, On the shape and size of the fracture zones on glass fracture surfaces, The Philosophical Magazine: A Journal of Theoretical Experimental and Applied Physics 14 (1966) 731–743.

[50] S. A. Ruggero, Quantitative fracture analysis of etched soda-lime silica glass: Evaluation of the blunt crack hypothesis, Ph.D. thesis, University of Florida Gainesville, FL, 2003.

[51] O. Gaume, S. Pelletier, Analysis of fracture features for uni-axial bent glass plates, Saint-Gobain Recherche, Technical Document (2013).

[52] M. Ball, R. Bradt, D. Landini, Fracture mist region in a soda-lime-silica float glass, ASTM International, 1984.

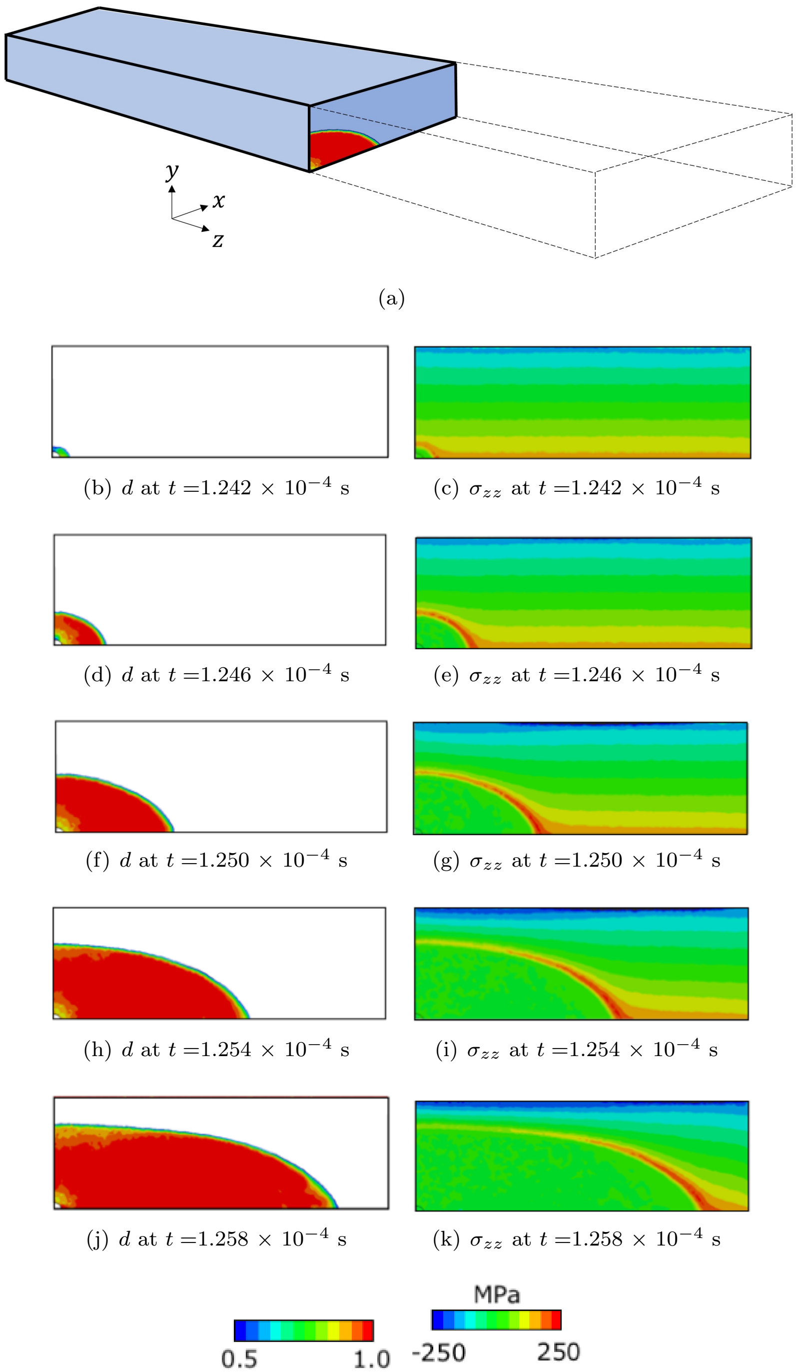

(a)

(b) d at $t = 1.242 \times 10^{-4}$ s

(c) σ_{zz} at $t = 1.242 \times 10^{-4}$ s

(d) d at $t = 1.246 \times 10^{-4}$ s

(e) σ_{zz} at $t = 1.246 \times 10^{-4}$ s

(f) d at $t = 1.250 \times 10^{-4}$ s

(g) σ_{zz} at $t = 1.250 \times 10^{-4}$ s

(h) d at $t = 1.254 \times 10^{-4}$ s

(i) σ_{zz} at $t = 1.254 \times 10^{-4}$ s

(j) d at $t = 1.258 \times 10^{-4}$ s

(k) σ_{zz} at $t = 1.258 \times 10^{-4}$ s

Fig. 9 Phase–field profile, d ((b), (d), (f), (h), and (j)) and stress profile, σ_{zz} ((c), (e), (g), (i), and (k)) in 2D for case 1 at the plane of symmetry, $z = 0$, at five time steps

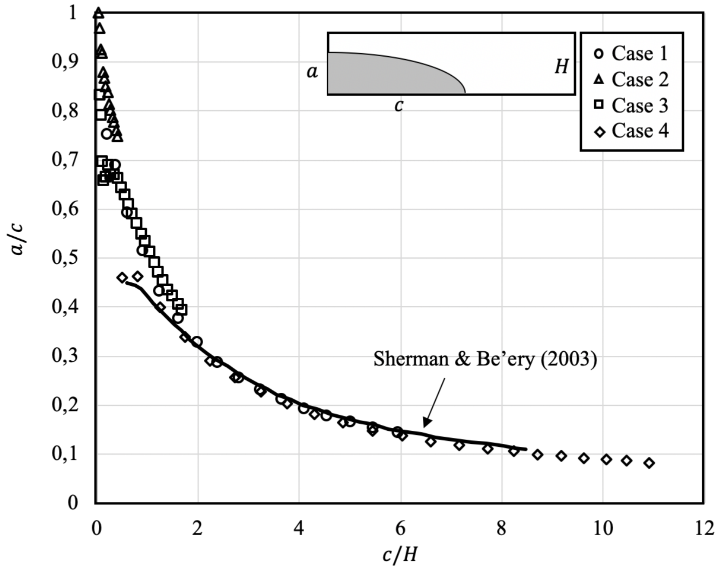

Fig. 10 Crack shape a/c versus c/H. Solid line corresponds to experimental results in Sherman & Be'ery [41]

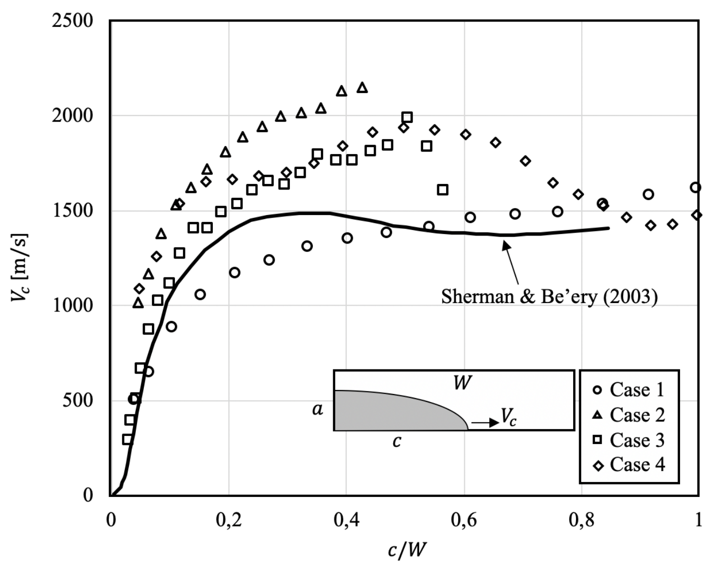

Fig. 11 Crack velocity, V_c, versus normalized crack length, c/W, along the free surface. Solid trend corresponds to experimental results in Sherman & Be'ery [41]

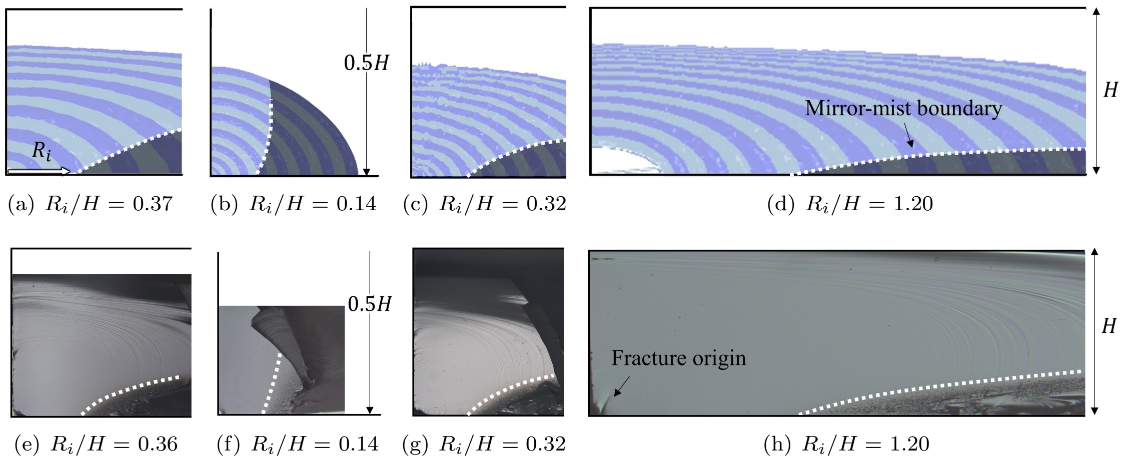

Fig. 12 Mirror–mist boundaries estimated by crack velocity and from experimental observation for cases 1 to 4

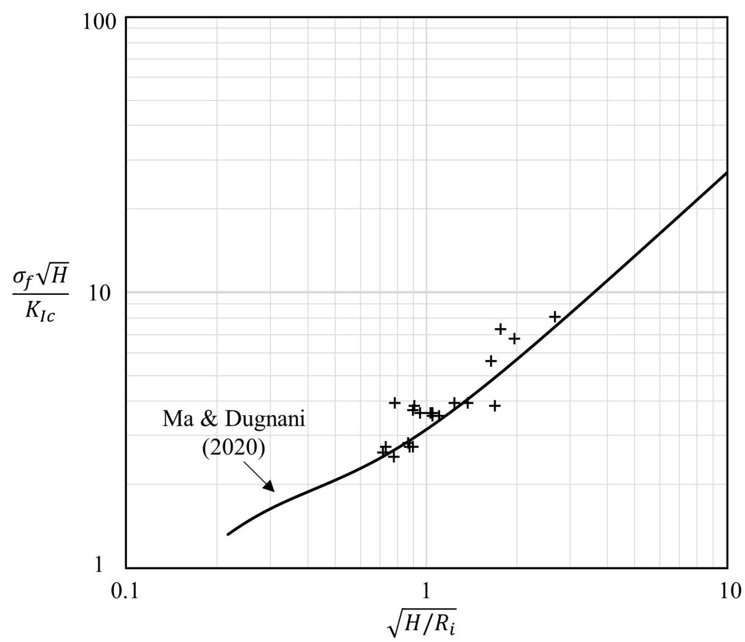

Fig. 13 Normalized strength, $\sigma_f\sqrt{H/K_{Ic}}$, versus $\sqrt{H/R_i}$ in logarithmic scale for twenty-one cases simulated. The expected trend proposed by Ma & Dugnani [5] is shown for reference

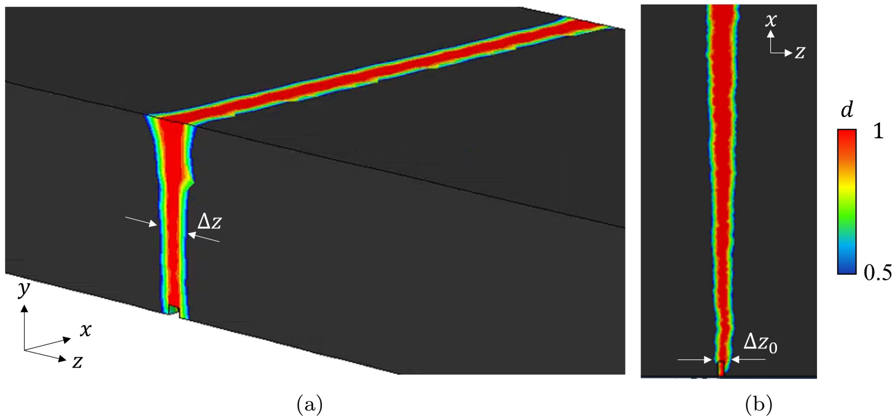

Fig. 14 Thickness of the damage area, Δz, with $d > 0.5$, in (a) 3D view and (b) 2D view at $y = 0$

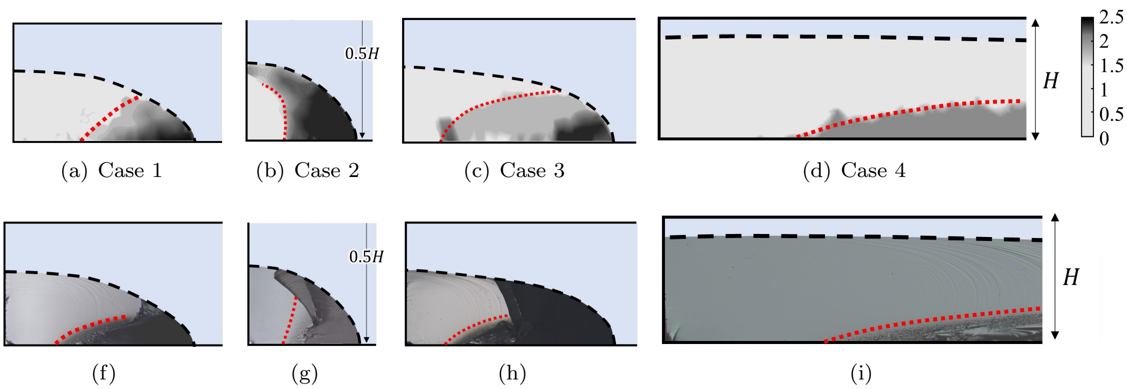

Fig. 15 (a-d) Normalized thickness of the damaged area, $\Delta z/\Delta z_0$, for cases 1 to 4, and (f-i) experimental fracture surface. Estimated mirror–mist boundary at $\Delta z/\Delta z_0$ =1.5 was shown in red dotted line

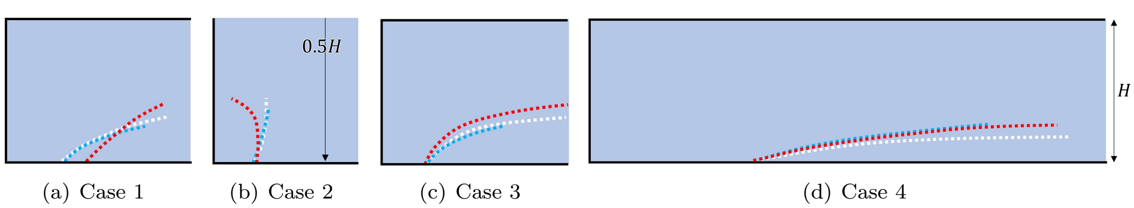

Fig. 16 Comparison between mirror–mist boundaries estimated by critical velocity (white), thickness of the damage area (red), and experimental observation (blue), for cases 1 to 4

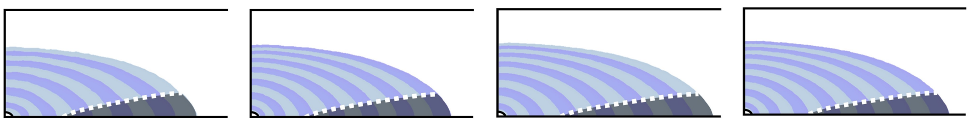

(a) $\ell/h = 1$ (b) $\ell/h = 2$ (c) $\ell/h = 4$ (d) $\ell/h = 8$

Fig. 17 Mirror–mist boundary estimated by crack velocity for various ℓ/h

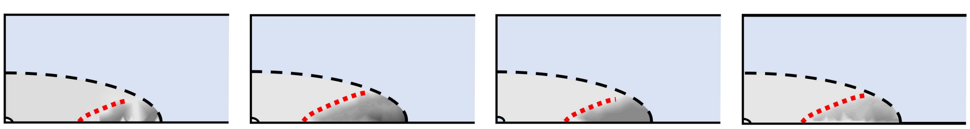

(a) $\ell/h = 1$ (b) $\ell/h = 2$ (c) $\ell/h = 4$ (d) $\ell/h = 8$

Fig. 18 Mirror–mist boundary estimated by the damaged area, $\Delta z/\Delta z_0$, for various ℓ/h. Color scale is the same as Figure 15